# A Method for Detecting Hidden Faults in Power Lines by Combining Visible and Thermal Infrared Images

Yuting Qin<sup>1</sup>, Yansong Duan<sup>1,\*</sup>

<sup>1</sup>School of Remote Sensing and Information Engineering, Wuhan University, Wuhan 430079, qinyuting@whu.edu.cn, ysduan@whu.edu.cn

Keywords: Power line inspection; Hidden faults; Component localization; Thermal infrared images; Image registration.

#### **Abstract**

Hidden faults in power lines pose significant safety hazards, severely threatening the safety of human life and property, necessitating rigorous inspection. Current methods for detecting hidden faults face two primary challenges: firstly, the inability to accurately locate power line components in thermal infrared images, and secondly, the reliance on empirical thresholds for fault determination, which results in low detection accuracy. To address these issues, this paper proposes a method for detecting hidden faults in power lines by combining visible and thermal infrared images. The method initially leverages the high discernibility of visible images to precisely identify the locations of power line components using a deep learning-based object detection model. Subsequently, a matching algorithm based on regional features is employed to register visible and thermal infrared images, thereby obtaining the precise locations of components in thermal infrared images. Finally, thermal infrared images are used to measure the temperature of components. By comparing these measured temperatures with the surface temperatures of components under normal operating conditions, hidden faults are effectively identified. Experiments were conducted on transmission lines in Jiashan County, Jiaxing City, Zhejiang Province. Out of 1526 power line components, 14 faults were detected, with manual verification confirming 13 as genuine faults. Compared to manual inspection results, the proposed method exhibited no missed detections and only one false positive, achieving a detection accuracy of 0.93.

### 1. Introduction

In recent years, with the rapid development of China's industrial sector, a substantial number of power lines have been put into operation. By the end of 2024, China's cumulative installed power generation capacity reached approximately 3.35 billion kilowatts, with the length of transmission lines at 220 kV and above exceeding 920,000 kilometers, ranking first globally in both total length and capacity. Transmission lines deliver electricity to end-users, and any faults can lead to significant inconveniences. Among these, hidden faults pose significant safety hazards, such as disruptions to industrial and household supply, paralysis of transportation and other infrastructure, fires caused by short circuits, and safety hazards from broken conductors, resulting in substantial losses. Therefore, to ensure the safe and stable operation of power lines, rigorous inspection and maintenance are essential (Wen et al., 2019).

To mitigate the safety risks posed by hidden faults, the primary objective is to accurately locate components. Currently, numerous studies have focused on component localization using visible light images (Liu et al., 2018; Chen et al., 2019; Wan et al., 2020; Liang et al., 2020; Xie et al., 2023; Souza et al., 2023; Stefenon et al., 2023). Leveraging deep learning-based object detection models, these methods can achieve high-precision localization of various components, which are applicable to the detection of surface faults such as missing top caps, insulator breakage, missing insulators, missing pins, foreign matters on towers, and conductor breakage. However, hidden faults are primarily caused by internal aging or loose connections, manifesting as temperature anomalies. These anomalies cannot be detected by visible images but can be captured by thermal infrared images. Unfortunately, due to the low contrast and poor detail resolution of thermal infrared images, existing methods struggle to achieve high-precision component localization in complex backgrounds. A promising approach is to combine

visible and thermal infrared images (Jalil et al., 2019), but this method faces two challenges: precise localization of components in visible images and reliable registration between visible and thermal infrared images. The first challenge can be addressed using state-of-the-art object detection models. As for the second challenge, although some research has been conducted on the registration of visible and infrared images, including region-based methods (Yang et al., 2009; Zhuang et al., 2016; Yu et al., 2019), feature-based methods (Wang et al., 2010; Aguilera et al., 2012; Yi et al., 2013; Zeng et al., 2020; Chen et al., 2020; Jiang et al., 2020), and deep learning-based methods (Zhao et al., 2017; Wang et al., 2018; Zhang et al., 2021; Mao and He, 2021), these methods remain immature. Given the complexity of power line inspection scenarios, existing methods cannot achieve fast and reliable registration, making them difficult to directly apply to this study.

Following component localization, the next challenge is hidden fault identification. Several studies have explored fault detection in power lines using thermal infrared images (He et al., 2015; Wronkowicz, 2016; Liu et al., 2017; Jalil et al., 2019; Wang et al., 2020). These methods typically calculate the surface temperatures of components from thermal infrared images and compare them with empirical thresholds, identifying components with temperatures exceeding the threshold as potential hidden faults. However, temperature measurements from thermal infrared images are influenced by environmental factors such as solar radiation, leading to deviations between measured and actual temperatures. Additionally, temperatures of components vary under different environmental conditions, including ambient temperature, solar irradiance, and power transmission energy, making it difficult to determine a temperature threshold. Therefore, accurate identification of hidden faults requires a robust model. However, most existing methods rely on empirical models, resulting in low detection accuracy and poor generalizability.

<sup>\*</sup> Corresponding author

To address these issues, this paper a novel approach to detecting hidden faults in power lines by combining visible and thermal infrared images. The method involves locating components using both visible and thermal infrared images, followed by temperature measurement of these components via thermal infrared images and estimation of their surface temperatures under normal operating conditions to identify hidden faults. For component localization, based on existing frameworks, a network model is designed to detect and locate components in visible images. Subsequently, image registration is performed to map these locations onto thermal infrared images. For hidden fault identification, a hybrid radiative temperature rise model is proposed, which fits temperature data from thermal infrared images and estimates the surface temperatures of components under normal conditions by considering environmental factors and transmission energy. By comparing measured and estimated temperatures, hidden faults can be identified.

The contributions of this paper are as follows:

- (1) A region-based image registration method for visible and thermal infrared images is proposed, improving the success rate of image matching.
- (2) A hybrid radiative temperature rise model that integrates environmental temperature, solar irradiance, and power line metadata is developed, enhancing the accuracy of hidden fault detection.
- (3) A comprehensive hidden fault identification technique combining object detection and image registration is introduced.

### 2. Methodology

To address the issues of existing methods in component localization and hidden fault identification, this paper proposes a method for detecting hidden faults in power lines by combining visible and thermal infrared images. The method initially leverages the high discernibility of visible images to precisely identify the locations of power line components using a deep learning-based object detection model. Subsequently, a matching algorithm based on regional features is employed to register visible and thermal infrared images, thereby obtaining the precise locations of components in thermal infrared images. Finally, thermal infrared images are used to measure the temperature of components. By comparing these measured temperatures with the surface temperatures of components under normal operating conditions, hidden faults are effectively identified. The technical framework of the proposed method is shown in Figure 1.

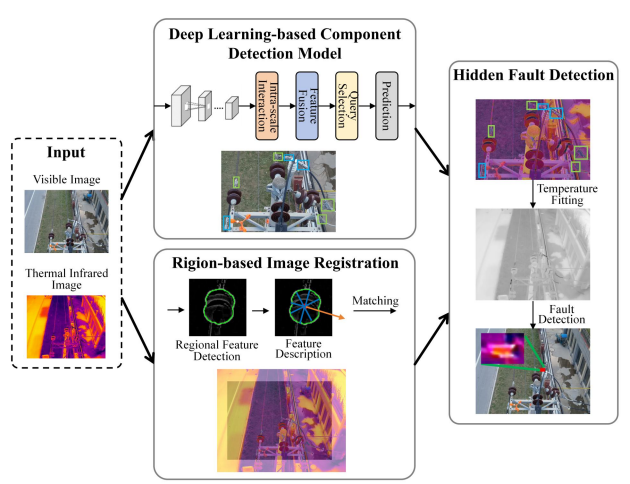


Figure 1. The technical framework of the proposed method

# 2.1 Component Localization Based on Visible and Thermal Infrared Images

Existing methods face substantial challenges in identifying and precisely locating components in thermal infrared images, particularly in complex scenarios. To address this issue, this paper proposes a high-precision localization method for components that combines visible and thermal infrared images. The proposed method initially leverages the high discernibility of visible images to identify and locate components such as insulators and joints using a deep learning-based object detection model. Then, regional features are extracted from both visible and thermal infrared images, followed by the construction of scale- and rotation-invariant feature descriptors. Through feature matching between the two image modalities, the precise locations of components in thermal infrared images can be accurately determined.

#### 2.1.1 Component Detection Model Based on RT-DETR

The primary objective of component detection is to identify and locate specific components, effectively distinguishing them from the background, which can be achieved through object detection. In this study, the detection of hidden faults in power lines necessitates the precise localization of components, thereby requiring object detection models with high detection accuracy, while simultaneously optimizing inference speed. Prominent algorithms in the field of object detection include the RCNN series, YOLO series, SSD series, and DETR series. In this paper, the RT-DETR model (Lv et al., 2023) was selected for component detection. This model represents the first real-time, end-to-end object detection model capable of maintaining high accuracy while achieving real-time detection speeds.

The network architecture of RT-DETR comprises a backbone network, an efficient hybrid encoder, and a Transformer decoder with auxiliary prediction heads, as shown in Figure 2.

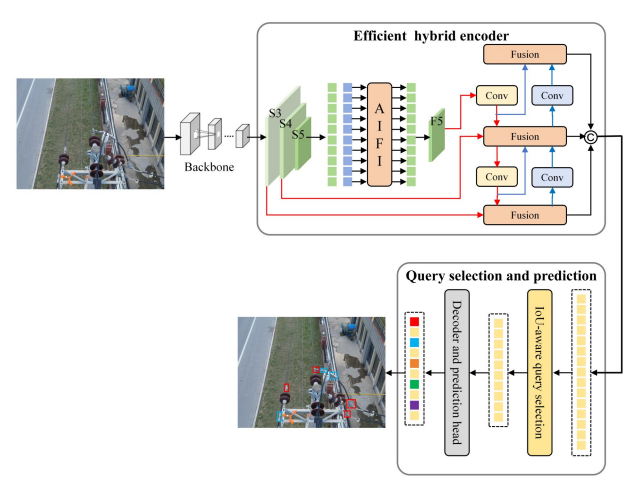


Figure 2. Network architecture of RT-DETR

Initially, the model employs the backbone network to extract features, retaining the output features from the last three stages {S3, S4, S5} as inputs to the hybrid encoder. Subsequently, the hybrid encoder transforms multi-scale features into a sequence of image features through intra-scale interaction (AIFI) and cross-scale feature-fusion module (CCFM), facilitating subsequent object query tasks. To enhance detection accuracy by providing more precise classification and localization encoder features for object queries, an IoU (Intersection over Union) aware query selection module is employed to select a

"Mobile Mapping for Autonomous Systems and Spatial Intelligence", 20–22 June 2025, Xiamen, China

fixed number of image features from the encoder output sequence as initial object queries for the decoder. Finally, the decoder with auxiliary prediction heads iteratively optimizes the object queries, generating prediction boxes and confidence scores. For detailed structures and functionalities of each module, refer to the original literature (Lv et al., 2023), which will not be reiterated here.

# 2.1.2 Region-based Image Registration Method for Visible and Thermal Infrared Images

To address the challenge of registering visible and thermal infrared images, inspired by the SIFT algorithm (Lowe, 2004), this paper proposes a region-based image registration algorithm. The algorithm begins by extracting regional features from both visible and thermal infrared images. It then calculates the principal direction and the normalized distances from the boundary to the centroid for each regional feature, thereby constructing scale- and rotation-invariant feature descriptors. Finally, the Euclidean distance is used as a similarity criterion to match corresponding regions. The specific process is as follows:

### (1) Regional Feature Detection

Feature detection aims to extract features with specific semantic structures from images, such as point features, line features, and regional features. The registration algorithm proposed in this paper is based on regional features. The objective of regional feature detection in this paper is to extract stable regions from images that preserve the boundaries of the original targets while also ensuring an adequate quantity. However, traditional regional segmentation algorithms, such as region growing, watershed algorithm, and saliency detection algorithms, fall short in terms of both the quality and quantity of regional feature extraction required for this research. Therefore, this paper turns to deep learning-based regional segmentation algorithms. Recently, Meta introduced a new image segmentation model, SAM (Segment Anything Model) (Kirillov et al., 2023), which is trained on extensive segmentation datasets and exhibits strong generalization capabilities. It can generate masks for targets in any image or video, even on entirely new datasets without additional training. Experiments confirm that the SAM model can effectively extract regional features from both visible and thermal infrared images. Thus, the SAM model is transferred to the regional feature detection task in this paper.

### (2) Regional Feature Description

After extracting image features, it is not feasible to directly match these features. Instead, the regions must be mapped into discriminant vectors to facilitate fast and convenient matching. The process of calculating feature vectors is known as feature description. The regional feature description process in this paper is similar to the SIFT algorithm. After extracting regional features using the SAM model, for each regional feature, the centroid is first determined. Principal Component Analysis (PCA) is then employed to calculate the principal direction. Finally, the normalized distances from the boundary to the centroid are computed to yield a feature vector that is invariant to rotation and scaling.

Considering the differences in recorded information between visible and thermal infrared images, the pixel center of the region is used as the centroid to avoid the impact of image grayscale on algorithm stability. The centroid is calculated as follows:

$$\begin{cases} \bar{x} = \frac{1}{N} \sum_{(x,y) \in R} x \\ \bar{y} = \frac{1}{N} \sum_{(x,y) \in R} y \end{cases}$$
 (1)

where

R = the set of points in the region

 $\bar{x}$ ,  $\bar{y}$  = the pixel coordinates of the centroid

x, y = the pixel coordinates of the current point

N = the number of points in the region

Determining the principal direction of the regional feature ensures the descriptor's rotational invariance. Unlike the SIFT algorithm, which uses pixel gradients from differential images to calculate the principal direction, this paper employs PCA to compute the principal direction to mitigate deviations caused by differences in recorded information between visible and thermal infrared images and to simplify calculations. In the actual calculation process, the covariance matrix of the coordinate matrix of the region is first calculated as follows:

$$\boldsymbol{C} = \begin{bmatrix} cov(\boldsymbol{X}, \boldsymbol{X}) & cov(\boldsymbol{X}, \boldsymbol{Y}) \\ cov(\boldsymbol{Y}, \boldsymbol{X}) & cov(\boldsymbol{Y}, \boldsymbol{Y}) \end{bmatrix}, \tag{2}$$

where

 $\boldsymbol{C}$  = covariance matrix

X, Y =two coordinate vectors of the coordinate matrix cov =covariance between two variables, it is calculated as follows:

$$cov(\boldsymbol{a},\boldsymbol{b}) = \frac{1}{n-1} \sum_{i=1}^{n} (a_i - \overline{a})(b_i - \overline{b}), \tag{3}$$

where

 $\boldsymbol{a}, \boldsymbol{b} = \text{two vectors}$ 

n = the length of the two vectors

 $a_i$ ,  $b_i$  = i-th elements of the two vectors

 $\bar{a}$ ,  $\bar{b}$  = sample means of the two vectors

After obtaining the covariance matrix of the region, it is decomposed to yield eigenvalues and eigenvectors. The eigenvector corresponding to the largest eigenvalue is identified as the principal direction of the regional feature. Once the principal direction is determined, rays are drawn from the centroid at 10-degree intervals, covering a 0 to 360-degree range, resulting in 36 rays. These rays intersect the regional boundary at 36 points, and the Euclidean distances from these boundary points to the centroid are calculated, as shown in Figure 3. The computed 36 distance values are filtered by removing the top 5% of maximum and minimum values and then normalized to yield the feature vector. Normalization ensures the descriptor's scale invariance.

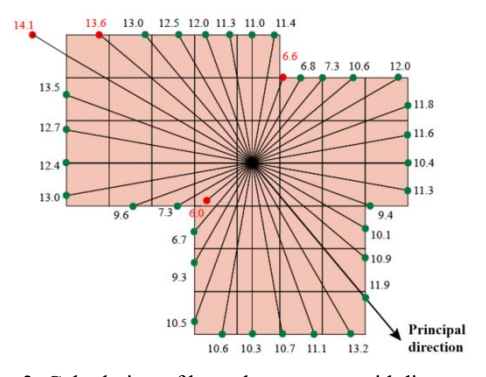


Figure 3. Calculation of boundary-to-centroid distances and normalized feature vector

### (3) Regional Feature Matching

Feature matching aims to correspond features extracted from two images. The descriptors constructed in this paper are presented in vector form, facilitating straightforward computation. Therefore, the Euclidean distance is chosen as the similarity criterion for feature matching. For two regions, if their distance is below a specified threshold, they are identified as corresponding regions. This process yields a set of matching points. Considering that similar regions on an image may produce similar regional features, leading to incorrect matches, the RANSAC algorithm (Fischler and Bolles, 1981) is employed to eliminate mismatched points.

### 2.2 Hybrid Radiative Temperature Rise Model

Existing methods for hidden fault identification often rely on empirical thresholds, resulting in low detection accuracy. To address this issue, this paper proposes a hybrid radiative temperature rise model that integrates multiple factors, including ambient temperature, humidity, solar irradiance, electric current, voltage, and resistance. The model first fits the surface temperatures of components using thermal infrared images, then establishes the relationship between temperature and component radiation through various influencing factors to estimate the surface temperatures of components under normal conditions, and finally compares the fitted and estimated temperatures to identify hidden faults.

# 2.2.1 Temperature Fitting Model Based on Thermal Infrared Images

Conventional temperature fitting methods often use linear or piecewise function models. However, these models do not account for the attenuation of radiant energy due to factors such as camera-object distance and humidity during the imaging process, leading to deviations between fitted and actual temperatures. Considering the effects of distance, humidity, and component emissivity, the radiant energy received by the thermal infrared camera at the entrance pupil per unit time is given by:

$$E = \frac{1}{2\pi} E_T \cdot r \cdot e^{-\alpha \cdot d} \frac{1}{\beta \cdot h + \gamma},\tag{4}$$

where E = radiant energy at the entrance pupil

 $E_T$  = radiant energy per unit area of the component per unit time

T =surface temperature of the component

r = energy proportion in the thermal infrared band

d = distance from the camera to the component

h = atmospheric relative humidity

 $\alpha$ ,  $\beta$ ,  $\gamma = constants$ 

The radiant energy at the entrance pupil can be calculated from the grayscale values of the thermal infrared image, and the relationship between the component's radiant intensity and surface temperature is given by the Stefan-Boltzmann law:

$$E_T = \varepsilon \cdot \sigma T^4,\tag{5}$$

where  $\varepsilon =$  emissivity of the component

 $\sigma$  = Stefan-Boltzmann constant

Through the above process, a relationship between the grayscale values of thermal infrared images and component temperatures is established. In practical applications, since camera calibration parameters are often unknown, radiance cannot be accurately calculated. Therefore, Equations (4) and (5) are combined and simplified, with all parameters except image grayscale values, distance, humidity, and temperature being calculated collectively, resulting in Equation (6):

$$I = a_0 + \frac{a_1 T^4 e^{-d}}{h + a_2},\tag{6}$$

where

I = image grayscale values $a_0, a_1, a_2 = \text{constants}$ 

# 2.2.2 Temperature Estimation Model Integrating Remote Sensing Information

After calculating the temperature of components, conventional methods typically use empirical thresholds to identify hidden faults. However, in different environments, temperature thresholds are often not fixed, making empirical models unreliable. To address this issue, the following processes are considered in temperature analysis: First, according to Joule's law, the resistance at connections is nearly zero under normal conditions, resulting in low thermal power; when components age or connections loosen, resistance increases significantly, leading to high thermal power and hidden faults. Second, for a component, factors contributing to temperature rise include not only its own thermal power but also absorbed radiation from surrounding objects and solar radiation. Therefore, under solar radiation, measured temperatures are higher than normal. Accordingly, this paper analyzes the radiant energy transmission process of components in the thermal infrared band, as shown in Figure 4.

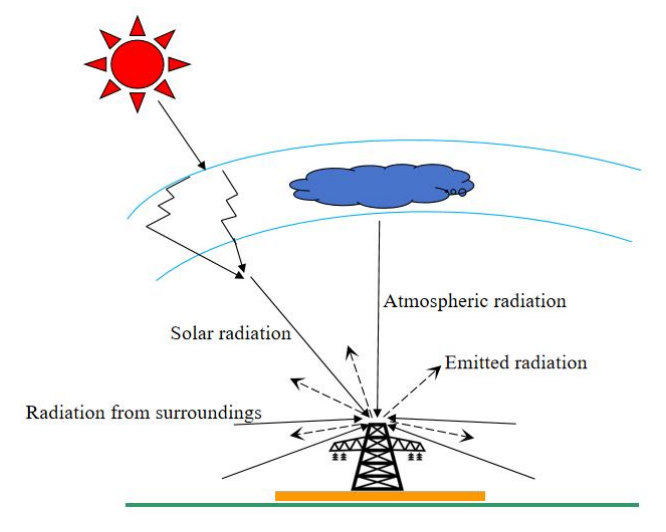


Figure 4. Radiant energy transmission process of components in the thermal infrared band

When ignoring the component's thermal power, solar radiation, and atmospheric radiation are not considered, the component's temperature equals the ambient temperature, and its radiant intensity is:

$$E_{T_0} = \varepsilon \cdot \sigma T_0^4,\tag{7}$$

where

 $E_{T_0}$  = radiant intensity  $T_0$  = ambient temperature Under solar radiation, the internal energy of components primarily comes from the following sources: radiation from surrounding objects, the component's thermal power, absorbed solar radiation and atmospheric downwelling radiation. At thermal equilibrium, this energy is emitted as heat transfer or longwave radiation. Neglecting heat transfer, the radiant intensity  $E_P$  due to the component's thermal power is:

$$E_P = P/S, (8)$$

where P =thermal power

S = surface area of the component

The thermal power is calculated as follows:

$$P = I^2 R = I^2 \frac{\rho L}{S_c},\tag{9}$$

where I = electric current

R = resistance

 $\rho$  = resistivity

L = length

 $S_c =$ cross-sectional area

The radiant intensity  $E_{\alpha}$  due to absorbed solar and atmospheric radiation is:

$$E_{\alpha} = (E_l \cdot \alpha_1 + E^{\downarrow} \cdot \alpha_2) \cdot S_l / S, \tag{10}$$

where  $E_l = \text{solar horizontal radiation}$ 

 $E^{\downarrow}$  = atmospheric downwelling radiation

 $\alpha_1$ ,  $\alpha_2$  = absorption rates

 $S_l$  = surface area of the component exposed to solar radiation

Thus, the total radiant intensity  $E_T$  of the component is:

$$E_T = E_{T_0} + E_P + E_{\alpha}, (11)$$

In practical applications, due to numerous unknown variables, the above equations are simplified, and a multiple linear regression model is used to describe the relationship between component's temperature and ambient temperature, component's thermal power, solar radiation, and atmospheric downwelling radiation, as follows:

$$T^4 = T_0^4 + b_1 P + b_2 E_I + b_3 E^{\downarrow}, \tag{12}$$

where  $b_0, b_1, b_2, b_3 = \text{constants}$ 

Additionally, when a component experiences a hidden fault, its resistance cannot be measured. Thus, this paper uses Equation (12) to estimate the normal surface temperatures of components and compares them with the fitted temperatures obtained from Equation (6) to identify hidden faults.

### 3. Experiments and Discussion

Experiments were conducted on transmission lines in Jiashan County, Jiaxing City, Zhejiang Province. The experimental arrangement of this paper is as follows: First, a dataset of power line components was constructed, and a deep learning-based object detection model was trained. Subsequently, visible and thermal infrared images were registered. The component detection results and registration outcomes were then combined to obtain the precise locations of components in thermal

infrared images. Finally, hidden faults were identified using the hybrid radiative temperature rise model.

#### 3.1 Dataset Description

The images used in the experiments were captured by UAVs during different periods, including April, September, and December. The dataset comprises 817 visible images and 245 thermal infrared images, with some examples shown in Figure 5. As depicted, the captured images feature complex backgrounds and contain multiple components of varying types, posing a challenge for object detection tasks.



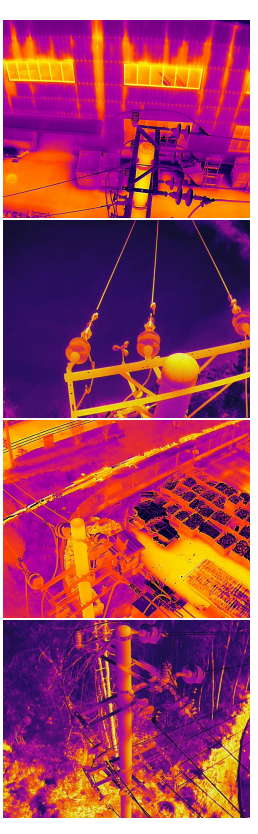


Figure 5. Sample images from the experimental dataset

## 3.2 Component Detection

Using the LabelImg tool, a total of 5,197 samples were annotated from the 817 visible images, encompassing 11 categories, including 6 types of joints and 5 types of insulators. The dataset was split into training and testing sets in a 7:3 ratio for training and evaluating the RT-DETR model.

The model was trained on a single GPU with a learning rate of 0.01 and a weight decay of 0.0005. The best training results were achieved after 247 epochs. The model was tested on the testing set, and precision-recall (PR) curves for each type of component were plotted, as shown in Figure 6. The average precision (AP) for each component was calculated by measuring the area under the curve, with higher AP indicating better model performance. As depicted, most components achieved high AP values. To evaluate the overall model performance, mAP@0.5 (the mean average precision when IoU (Intersection over Union) was equal to 0.5) was computed, yielding a value of 0.943. Overall, the model demonstrated high detection accuracy, meeting the requirements of this paper.

"Mobile Mapping for Autonomous Systems and Spatial Intelligence", 20–22 June 2025, Xiamen, China

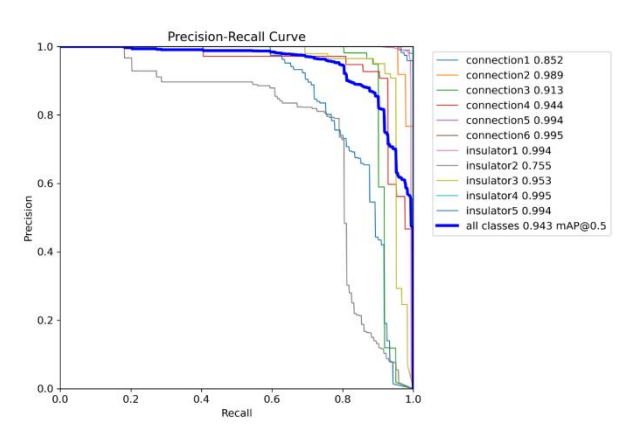


Figure 6. PR curves for each type of component

## 3.3 Registration of Visible and Thermal Infrared Images

The proposed registration method was applied to 245 pairs of visible and thermal infrared images from the dataset, with some results shown in Figure 7. As depicted, the matched keypoints align well with the actual scenarios. Additionally, the average registration precision (proportion of correctly matched points) was calculated, resulting in a value of 0.863. These results validate the effectiveness of the proposed method.

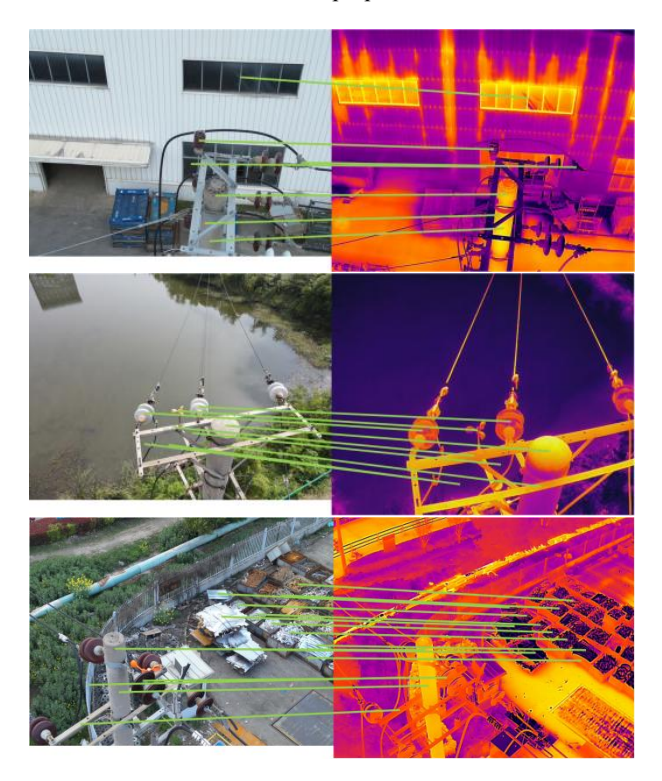


Figure 7. Sample registration results

The proposed registration algorithm was compared with several classical methods, including the SIFT algorithm, SURF algorithm (Bay et al., 2006), deep learning-based method SuperGlue (Sarlin et al., 2020), multimodal image registration methods OS-SIFT (Xiang et al., 2018) and RIFT (Li et al., 2019). The average registration precision of each method was statistically analyzed, and the results are presented in Table 1. As shown in the table, the proposed method demonstrates superior registration precision compared to traditional approaches SIFT and SURF while achieving comparable performance to SuperGlue, OS-SIFT, and RIFT. The

experimental results validate the feasibility and reliability of the proposed method.

Method Precision	SIFT 0.079	SURF 0.052	SuperGlue 0.847
Method	OS-SIFT	RIFT	Ours
Precision	0.861	0.874	0.863

Table 1. Comparison of registration precision between the proposed method and several classical methods

# 3.4 Localization of Components in Thermal Infrared Images

Experiments were conducted using 245 pairs of visible and thermal infrared images to locate power line components, with partial results shown in Figure 8. The locations in visible images represent the object detection results, while the locations in thermal infrared images depict the components mapped onto thermal infrared images after registration. Visually, the localization results align well with the actual scenarios, demonstrating high accuracy without any missed detections.

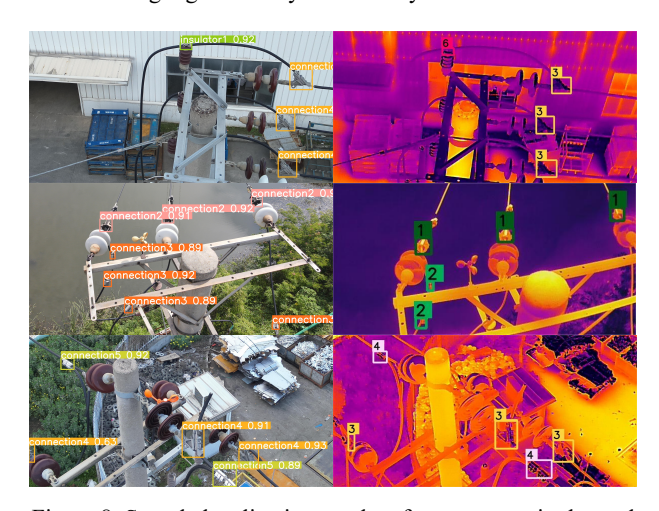


Figure 8. Sample localization results of components in thermal infrared images

### 3.5 Hidden Fault Detection

In Section 2, a hybrid radiative temperature rise model was proposed, including temperature fitting and normal temperature estimation. For temperature fitting, during one process of acquiring thermal infrared images, the temperatures of 21 objects were measured synchronously. Six measurements were used to calculate the parameters, and the remaining 15 measurements were used to validate the model. The fitted temperatures were compared with the measurements, as shown in Table 2. The root mean square error (RMSE) of the fitting results was 0.96 °C, with a goodness-of-fit (R²) of 0.939, indicating excellent fitting performance. The fitting errors were within 2 °C, satisfying practical application requirements.

Equation (12) was used for normal temperature estimation. A total of 84 data points were measured to fit the regression model, resulting in an RMSE of 1.19 °C and an R<sup>2</sup> of 0.926.

Furthermore, to quantitatively evaluate the influence of each independent variable on the dependent variable, t-tests were conducted. In statistical analysis, a significance threshold (typically 0.05, 0.02, or 0.01) is established to evaluate the linear relationship between variables. A P-value exceeding this

threshold indicates an insignificant linear relationship. In our experiments, all obtained P-values were below 0.01, confirming statistically significant linear relationships between each independent variable and the dependent variable. These results validate the correctness of the proposed model.

	Fitted temperatures (°C)	Measured temperatures (°C)
1	34.83	35.04
2	32.91	32.45
3	38.06	37.58
4	35.31	36.23
5	33.25	33.88
6	31.94	32.68
7	34.54	34.97
8	48.09	47.12
9	38.78	37.59
10	34.89	34.85
11	37.55	39.06
12	33.02	34.78
13	44.29	43.77
14	38.14	39.73
15	35.27	36.23

Table 2. Comparison of fitted and measured temperatures

For the 1,526 components in the 245 thermal infrared images, Equation (6) was used to fit their temperatures. For each component, its fitted temperature  $T_m$  was compared to a temperature threshold. If  $T_m$  exceeded the threshold, the component was identified as having a hidden fault. Following the methodology of Wang et al. (2020), the temperature threshold was set at 1.2 times normal temperature  $T_n$  of the component, where  $T_n$  is calculated using Equation (12). Based on this approach, 14 faults were detected, with some results shown in Figure 9. Additionally, manual inspection of the images revealed 13 hidden faults. Compared to the manual inspection results, the proposed detection method achieved no missed detections and only one false detection, yielding a detection accuracy of 0.93. In contrast, the conventional empirical threshold method identified 15 faults among the same 1526 components, but with lower performance: only 12 true positives, 3 false positives, and 1 false negative (precision = 0.80). The proposed method demonstrates superior performance, exhibiting both higher recall and improved detection accuracy compared to the conventional approach.

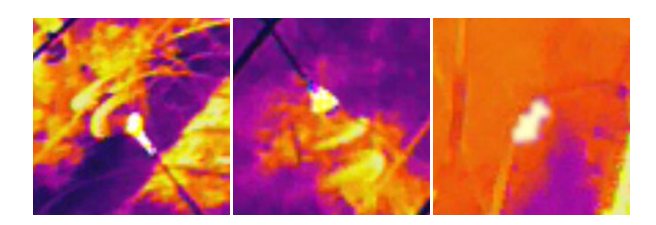


Figure 9. Sample hidden fault detection results

### 4. Conclusion

To address the limitations of existing methods in hidden fault detection, such as the inability to accurately locate power line components and the low precision in identifying hidden faults, this paper proposes a novel approach for detecting hidden faults in power lines by combining visible and thermal infrared images. Experimental results validate the effectiveness of the proposed method, offering a solution to the constraints of traditional methods. Compared to conventional approaches, the proposed method offers several advantages. First, it ensures

high recall in detecting components in thermal infrared images while simultaneously improving precision. Second, by establishing the relationship between temperature and component radiation through multiple influencing factors, it enables high-accuracy identification of hidden faults within power lines. This method has the potential to improve power line inspection systems and contribute to the safety of people and property. By accurately identifying hidden faults, we can mitigate disasters caused by power line failures. Furthermore, the proposed method holds significant implications for meeting the demands of automated detection in large-scale transmission systems and adapting to the rapid development of the economy and society.

#### Acknowledgements

This study was supported by National Key Research and Development Program of China, No. 2023YFB3905704.

#### References

Aguilera C, Barrera F, Lumbreras F, et al. 2012. Multispectral image feature points[J]. Sensors, 12(9): 12661-12672.

Bay H, Tuytelaars T, Van Gool L. 2006. Surf: Speeded up robust features[C]//European Conference on Computer Vision, 404-417.

Chen J, Xu X, Dang H. 2019. Fault Detection of Insulators Using Second - order Fully Convolutional Network Model[J]. Mathematical Problems in Engineering, 2019(1): 6397905.

Chen X, Liu L, Zhang J, et al. 2020. Registration of multimodal images with edge features and scale invariant PIIFD[J]. Infrared Physics & Technology, 111: 103549.

Fischler M A, Bolles R C. 1981. Random sample consensus: a paradigm for model fitting with applications to image analysis and automated cartography[J]. Communications of the ACM, 24(6): 381-395.

He S, Yang D, Li W, et al. 2015. Detection and fault diagnosis of power transmission line in infrared image[C]//2015 IEEE International Conference on Cyber Technology in Automation, 431-435.

Jalil B, Leone G R, Martinelli M, et al. 2019. Fault detection in power equipment via an unmanned aerial system using multi modal data[J]. Sensors, 19(13): 3014.

Jiang Q, Liu Y, Yan Y, et al. 2020. A contour angle orientation for power equipment infrared and visible image registration[J]. IEEE Transactions on Power Delivery, 36(4): 2559-2569.

Kirillov A, Mintun E, Ravi N, et al. 2023. Segment anything[C]//Proceedings of the IEEE/CVF International Conference on Computer Vision, 4015-4026.

Li J, Hu Q, Ai M. 2019. RIFT: Multi-modal image matching based on radiation-variation insensitive feature transform[J]. IEEE Transactions on Image Processing, 29: 3296-3310.

Liang H, Zuo C, Wei W. 2020. Detection and evaluation method of transmission line defects based on deep learning[J]. IEEE Access, 8: 38448-38458.

- Liu Y, Pei S, Fu W, et al. 2017. The discrimination method as applied to a deteriorated porcelain insulator used in transmission lines on the basis of a convolution neural network[J]. IEEE Transactions on Dielectrics and Electrical Insulation, 24(6): 3559-3566.
- Liu X, Jiang H, Chen J, et al. 2018b. Insulator detection in aerial images based on faster regions with convolutional neural network[C]//2018 IEEE 14th international conference on control and automation (ICCA). IEEE, 1082-1086.
- Lowe D G. 2004. Distinctive image features from scale-invariant keypoints[J]. International journal of computer vision, 60: 91-110.
- Lv W, Xu S, Zhao Y, et al. 2023. Detrs beat yolos on real-time object detection[J]. arXiv preprint arXiv:2304.08069.
- Mao Y, He Z. 2021. Dual-Y network: infrared-visible image patches matching via semi-supervised transfer learning[J]. Applied Intelligence, 51(4): 2188-2197.
- Sarlin P E, DeTone D, Malisiewicz T, et al. 2020. Superglue: Learning feature matching with graph neural networks[C]//Proceedings of the IEEE/CVF conference on computer vision and pattern recognition, 4938-4947.
- Souza B J, Stefenon S F, Singh G, et al. 2023. Hybrid-YOLO for classification of insulators defects in transmission lines based on UAV[J]. International Journal of Electrical Power & Energy Systems, 148: 108982.
- Stefenon S F, Singh G, Souza B J, et al. 2023. Optimized hybrid YOLOu Quasi ProtoPNet for insulators classification[J]. IET Generation, Transmission & Distribution, 17(15): 3501-3511.
- Wan X, Song H, Luo L, et al. 2019. Application of convolutional neural networks in pattern recognition of partial discharge image[J]. Power Syst. Technol, 43(6): 2219-2226.
- Wan N, Tang X, Liu S, et al. 2020. Transmission line image object detection method considering fine-grained contexts[C]//2020 IEEE 4th Information Technology, Networking, Electronic and Automation Control Conference (ITNEC). IEEE, 1: 499-502.
- Wang B, Wu D, Lu Q, et al. 2010. A new image registration method for infrared images and visible images[C]//2010 3rd International Congress on Image and Signal Processing. IEEE, 4: 1745-1749.
- Wang L, Gao C, Zhao Y, et al. 2018. Infrared and visible image registration using transformer adversarial network[C]//2018 25th IEEE International Conference on Image Processing (ICIP). IEEE, 1248-1252.
- Wang B, Dong M, Ren M, et al. 2020. Automatic fault diagnosis of infrared insulator images based on image instance segmentation and temperature analysis[J]. IEEE Transactions on Instrumentation and Measurement, 69(8): 5345-5355.
- Wronkowicz A. 2016. Approach to automated hot spot detection using image processing for thermographic inspections of power transmission lines[J]. Diagnostyka, 17.

- Xiang Y, Wang F, You H. 2018. OS-SIFT: A robust SIFT-like algorithm for high-resolution optical-to-SAR image registration in suburban areas[J]. IEEE Transactions on Geoscience and Remote Sensing, 56(6): 3078-3090.
- Xie Z, Fu M, Liu X. 2023. Electrical Fittings Inspection Based on Improved Unet with Generative Adversarial Network and Attention Mechanism[C]//2023 8th International Conference on Image, Vision and Computing (ICIVC). IEEE, 776-782.
- Yi X, Wang B, Fang Y, et al. 2013. Registration of infrared and visible images based on the correlation of the edges[C]//2013 6th International Congress on Image and Signal Processing (CISP). IEEE, 2: 990-994.
- Yu K, Ma J, Hu F, et al. 2019. A grayscale weight with window algorithm for infrared and visible image registration[J]. Infrared Physics & Technology, 99: 178-186.
- Yang Z, Shen G, Wang W, et al. 2009. Spatial-spectral cross correlation for reliable multispectral image registration[C]//2009 IEEE Applied Imagery Pattern Recognition Workshop (AIPR 2009). IEEE, 1-8.
- Zeng Q, Adu J, Liu J, et al. 2020. Real-time adaptive visible and infrared image registration based on morphological gradient and C\_SIFT[J]. Journal of Real-Time Image Processing, 17: 1103-1115.
- Zhao Z, Zhao L, Qi Y, et al. 2017. Infrared and visible image registration based on hypercolumns[C]//Computer Vision: Second CCF Chinese Conference, CCCV 2017, 529-539.
- Zhang X, He Z, Ma Z, et al. 2021. Llfe: A novel learning local features extraction for uav navigation based on infrared aerial image and satellite reference image matching[J]. Remote Sensing, 13(22): 4618.
- Zhuang Y, Gao K, Miu X, et al. 2016. Infrared and visual image registration based on mutual information with a combined particle swarm optimization Powell search algorithm[J]. Optik, 127(1): 188-191.